

FLOWFIELD MEASUREMENTS ABOUT AN AIRFOIL WITH LEADING-EDGE ICE SHAPES

Andy P. Broeren,^{*} Harold E. Addy, Jr.,[†] and Michael B. Bragg[‡]

University of Illinois at Urbana-Champaign, Urbana, Illinois, 61801
NASA Glenn Research Center at Lewis Field, Cleveland, Ohio 44135

ABSTRACT

Flowfield measurements were carried out on the upper surface of a GLC-305 airfoil configured with glaze and rime ice-shape simulations. The mean and root-mean-square fluctuation of the streamwise velocity were measured using a split-hot-film probe at several chordwise locations. These data were taken at three different angles of attack preceding stall for each iced-airfoil configuration at Reynolds numbers of 3.5×10^6 and 6.0×10^6 with Mach numbers of 0.12 and 0.21. The velocity measurements confirmed the presence of a large separation bubble downstream of the ice shapes. The separation bubbles for the glaze ice configuration were much larger than those for the rime ice case, resulting from the differences in the ice horn geometry. Other than the differences in size, the integral boundary-layer characteristics were very similar. Changes in Reynolds number did not significantly affect the separation bubble characteristics. However, a larger Mach number did result in a slightly larger separation bubble for the glaze ice case at $\alpha = 6$ deg. The root-mean-square velocity distributions had peak values in the separated shear layer, downstream of transition, that compared well with previous work.

NOMENCLATURE

c	Airfoil chord length
C_l	Lift coefficient
$C_{l,max}$	Maximum lift coefficient, coincident with α_{stall}
C_p	Pressure coefficient
M	Freestream Mach number
Re	Reynolds number based on chord
u	Time-averaged (mean) streamwise velocity
u_{rms}	Root-mean-square velocity fluctuation
U_e	Boundary-layer edge velocity
U_∞	Freestream velocity
x	Chordwise distance along airfoil
y	Distance normal to airfoil chord

y_{div}	Normal location of dividing stream line
y_{surf}	Normal location of airfoil surface
α	Airfoil angle of attack
α_{stall}	Stalling angle of attack, coincident with $C_{l,max}$
δ	Boundary-layer edge location (thickness)
δ^*	Boundary-layer displacement thickness
θ	Boundary-layer momentum thickness

INTRODUCTION

Large, leading-edge ice accretions on airfoils cause significant performance effects such as reduced lift and increased drag. The effects are well documented for a number of ice shape families.¹⁻³ Perhaps less understood, however, are the complex flowfield details associated with the ice accretion/airfoil geometry. An understanding of the flowfield is important for computational modeling used to predict the important performance losses. Knowledge of the iced-airfoil flowfield is also critical in determining what geometric degradations of the ice contribute to the performance degradations and how these may differ for other airfoils.

Typically, large glaze ice accretions on airfoils are characterized by "horns" that protrude some distance off the airfoil surface into the oncoming flow. These flowfields have been studied in previous work and a basic understanding of the time-averaged characteristics has been developed. The ice horn causes the flow to separate and for low angles of attack, the separated shear layer reattaches some distance downstream forming a separation bubble aft of the ice shape. It is possible that the reattached boundary layer, downstream of the bubble may separate again upstream of the airfoil trailing edge. In this case there are two separated flow regions of importance. For large glaze ice shapes, the separation bubble has a large, global effect on the pressure distribution.³ These are referred to as "long bubbles" as originally described by Tani⁴ for clean airfoils. Rime ice shapes tend to differ from

^{*}Research Scientist, Department of Aerospace Engineering, University of Illinois, Member AIAA.

[†]Research Engineer, Icing Branch, NASA Glenn Research Center at Lewis Field, Member AIAA.

[‡]Professor and Head, Department of Aerospace Engineering, University of Illinois, Associate Fellow AIAA.

glaze ice shapes in that usually there are no “horns” protruding into the flow. However, flow separation does occur because of discontinuities between the ice shape and airfoil surface.³ Depending upon the size of the ice shape, these bubbles may have a small, local effect on the pressure distribution and would thus be “short” using Tani’s definition.

This understanding of iced-airfoil separation bubbles has been developed over the last twenty years (or so) of icing research. The flowfield research included simple experimental methods such as flow visualization, detailed experimental methods such as hot-wire/film anemometry, or laser velocimetry and computational methods. Bragg, Khodadoust and Spring,⁵ performed split-hot-film anemometry measurements in the separation bubble flowfield about a simulated glaze ice accretion on the leading edge of a NACA 0012 airfoil. Both upper and lower surface separation bubble characteristics were measured. The overall results were consistent with the description given in the preceding paragraph. These measurements were performed at a low Reynolds number of 1.5×10^6 and a Mach number of 0.12. The results showed how the bubble grew in size as the airfoil angle of attack increased up to maximum lift. The largest bubble measured covered over 30% of the chord at angle of attack one degree below stall. An important result of this work was that the time-averaged separation bubble characteristics compared favorably to laminar separation bubbles that can form on uncontaminated, or clean, airfoils. Khodadoust⁶ performed laser-Doppler velocimeter (LDV) measurements on a straight rectangular wing with a leading-edge ice accretion having the same geometry. The earlier split-film data closely agreed with the non-intrusive LDV measurements and CFD calculations. In addition to the quantitative measurements, Khodadoust used a surface-oil method to visualize separation bubble reattachment features. This work was extended to an iced-swept-wing configuration and employed both LDV and helium bubble flow visualization.^{7,8} These data showed that the leading-edge separation caused a strong spanwise vortex on the swept wing. This also confirmed what had been observed in CFD calculations.

While the time-averaged characteristics of large ice shape induced separation bubbles are fairly well known, the unsteady characteristics are less certain. Bragg *et al.*⁵ performed some time-dependent measurements as a part of their study and report a low-frequency oscillation in the separation bubble flowfield. Gurbachi and Bragg⁹ have considered unsteady characteristics in more detail. A NACA 0012 airfoil model instrumented with high-frequency response pressure transducers (Kulites) was tested with both rime and glaze ice

simulations. The time-dependent pressure distributions indicated large-scale flow fluctuations. Spectral analysis of the data performed later indicated flow frequencies similar to that measured by Bragg *et al.*⁵

A motivation for work in this area is to provide data for improvement of computational results. Several studies have noted that the complexity of the flowfield and potential for large-scale unsteadiness may render some computational methods incapable of correctly modeling the flows. For example, Dunn *et al.*¹⁰ and Pan *et al.*¹¹ both suggest that accurate prediction of stalling angle and maximum lift for airfoils with large ice shapes requires unsteady, three-dimensional methods. Chung and Addy¹² suggest that more flowfield measurements should be made in order to better assess the predictive capabilities of current CFD methods for iced-airfoil calculations.

The present investigation directly addresses the latter suggestion. Time-averaged flowfield velocity measurements were carried out on the upper surface of a GLC-305 airfoil with both a rime and glaze ice-shape simulation. Performance measurements for this airfoil with the simulated ice shapes were carried out in previous experiments and thus the additional flowfield information provides for a comprehensive data set.¹³ A key conclusion from the previous testing was that large changes in Reynolds number had very little effect on the iced-airfoil performance. The objectives of the present investigation were to measure the time-averaged flowfield velocities on the iced-airfoil upper surface at several angles of attack for two different ice shapes. Split-hot-film anemometry was used to determine the streamwise velocity profiles at several chordwise locations along the airfoil upper surface. The measurements were performed in a pressure tunnel at Reynolds numbers of 3.5×10^6 and 6.0×10^6 at Mach numbers of 0.12 and 0.21 to investigate these effects.

EXPERIMENTAL METHODS

All aerodynamic testing was carried out at NASA Langley Research Center, using the Low-Turbulence Pressure Tunnel (LTPT). The LTPT is a closed-return wind-tunnel that is principally used for two-dimensional airfoil testing and is described in detail in references 14 and 15. It can be operated at stagnation pressures from near vacuum to 147 psia (except 15 to 20 psia) and over a Mach number range of 0.05 to 0.40. A heat exchanger and nine turbulence reduction screens are located in the inlet settling chamber. The contraction ratio is 17.6:1 and the test section dimensions are 36-inches wide by 90-inches high by 90-inches long. The tunnel was designed for two-

dimensional airfoil testing with model chord lengths up to 36-inches.¹⁴ The freestream turbulence intensity levels were about 0.1% or less for the operating conditions used in this investigation.¹⁵

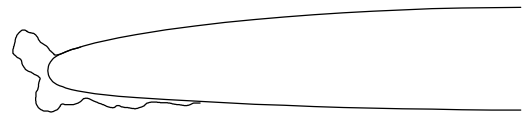
The GLC-305 airfoil model had a 36-inch chord by 36-inch span and was mounted horizontally across the width of the test section. The model was machined aluminum and had removable leading-edge sections. The leading-edge sections allowed for the various ice-shape simulations to be attached to the airfoil model. Two ice-shape simulations were used in this investigation and are shown in Fig. 1. The contour of these ice simulations was determined from smoothed coordinates of an ice tracing. These simulations were built from a laser-sintering rapid-prototyping method and had a constant cross-section in the spanwise direction. More details about the model, ice shapes and tunnel installation for aerodynamic performance measurements can be found in reference 13.

The flowfield mapping experiments required the addition of a significant amount of equipment both inside and outside of the test section. The existing boundary-layer measurement apparatus was adapted from previous testing.¹⁶ The traversing mechanism was mounted to the east wall of the test-section as shown in Fig. 2. A motor equipped with optical encoder feedback was used to control the vertical position of the measurement probes. This vertical traverse was cantilevered from the sidewall turntable via a track plate. The vertical positioning was computer controlled and provided a positioning accuracy of ± 0.0003 -inches. The track plate allowed the vertical traverse to be positioned in the chordwise direction. An operator remotely controlled the chordwise positioning based on feedback from a potentiometer that was routinely calibrated during the test. The chordwise position was set to within $\pm 0.003 x/c$. For the majority of chordwise locations the vertical traverses were performed in a direction normal to the chord line. There were some locations, near the leading edge, where the surface curvature required a small tilt angle. The tilt angle was also controlled remotely and measured by visual inspection of a vernier scale on the traverse apparatus. These angles were small (less than 10 deg.) and no correction to the streamwise velocity component was performed. The spanwise location of the measurement plane was fixed at 25% span (9 in.) from the side wall. The airfoil model had a row of surface static pressure orifices located at this spanwise station. These taps allowed for direct measurement of the airfoil pressure distribution directly below the traversing mechanism.

Two measurement probes were used. A TSI, Inc. model 1288 split-film probe was used for all of the data acquisition. This was a 0.006-inch diameter platinum



Smoothed 16.7-minute Rime Ice Shape 212



Smoothed 22.5-minute Glaze Ice Shape 944

Fig. 1 Smoothed ice shapes, after Addy *et al.*¹³

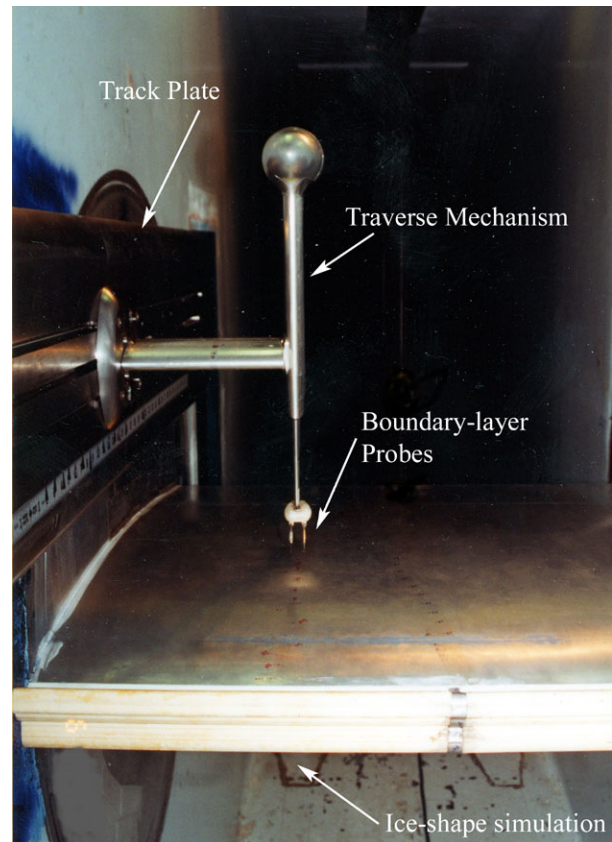


Fig. 2 Photograph of boundary-layer measurement apparatus installed in LTPT test section.

film mounted on a fiber rod. The plane of the split was oriented normal to the model chord (when the traverse axis was not tilted). This orientation of the split-film provided the magnitude and direction of the streamwise velocity component. The magnitude (but not direction) of the normal velocity was also obtained with this sensor. In addition, data from a flattened stagnation pressure probe were also acquired. The flattened tip of the pressure probe had a width of 0.010 inches. These data were only valid in non-reverse flow regions and were included only as an additional method to identify the boundary-layer edge and compare to the split-film data in regions where no reverse flow was present. The pressure probe was also used as part of an electrical contact circuit. The contact circuit sensed when the pressure probe contacted the airfoil surface. Based upon this location, the split-film sensor was positioned between 0.005 and 0.015-inches above the surface. This offset distance was regularly measured and applied to the velocity profile data.

Since the purpose of this investigation was to survey the flowfields of two iced-airfoil configurations over several Reynolds and Mach number conditions, time constraints prohibited detailed study of the separated flowfields. This limited the number of chordwise locations where the velocity profiles were acquired. In general, profiles were acquired every $0.03 x/c$ near the leading edge (up to $x/c = 0.15$), and then every $0.05 x/c$ farther downstream to the expected shear-layer reattachment region. Downstream of the expected reattachment region profiles were acquired every 0.10 to $0.25 x/c$. The spacing of points in the vertical direction was adjusted based on the thickness of the separation bubble or boundary layer. The profiles consisted of 25 to 40 points that had a non-linear distribution with closer spacing near the airfoil surface. For the glaze ice shape configuration 944, these velocity profiles were acquired at $\alpha = 0, 4$ and 6 deg. for $Re = 3.5 \times 10^6$ and 6.0×10^6 at constant $M = 0.12$. A subset of the velocity profiles was also acquired at $Re = 6.0 \times 10^6$ and $M = 0.21$. For the rime ice shape configuration 212, the velocity profiles were acquired at $\alpha = 6, 8$ and 10 deg. for $Re = 3.5 \times 10^6$ and 6.0×10^6 at constant $M = 0.12$.

The dual-sensor split-film probe was configured to measure the magnitude and direction of the streamwise velocity component. This method and data reduction procedures are described by Bragg *et al.*⁵ and Spring.¹⁷ The calibration of the sensor was performed in a 4-inch diameter ejector-driven flow facility that was located within the plenum of the LTPT. The Reynolds and Mach number combinations required two separate calibrations corresponding to two stagnation pressures. During each calibration the plenum pressure was set to

each of these stagnation pressures. In this way, each calibration was performed with the appropriate air density and minimal correction of the data was required. The calibration data were fit with polynomials using a least-squares method. Several calibrations were performed during the test to ensure that there was no drift due to sensor contamination or other effects. The velocity data are estimated to have uncertainties of a few percent of the freestream velocity. This estimate is based on the calibration repeatability and comparison of the split-film velocity data to that determined from the pressure probe.

Since the purpose of this investigation was to survey the flowfields of two iced-airfoil configurations over several Reynolds and Mach number conditions, time constraints limited the amount of data that could be acquired during each velocity profile. For each measurement point, 3000 split-film voltage samples were acquired at a rate of 1000 samples per second. This limited the bandwidth to a low-pass filter cut-off of 500 Hz. The voltages were temperature corrected (to account for differences in temperature during the data runs versus calibration) and the calibration was applied. The resulting velocities were then corrected for any minor difference in density between the data run and calibration. No corrections were applied for potential probe support interference effects. While it is likely that some interference effects were present, no suitable correction methods were found that were applicable to this experiment. It should also be noted that Khodadoust⁶ performed non-intrusive LDV measurements that compared very well with previous split-film measurements for the same iced-airfoil geometry, further indicating that interference effects were small.

The mean streamwise velocity (u) and root-mean-square of the velocity fluctuation (u_{rms}) were calculated from the time series data. The mean velocity profiles were used to calculate several boundary-layer parameters. These calculations were carried out using methods similar to Bragg *et al.*⁵ The stagnation streamlines were defined by the height above the airfoil surface in each profile where the streamwise velocity was zero. The dividing streamlines were defined by the height above the airfoil surface where the integrated mass flow (in the streamwise direction) was zero. This location, y_{div}/c , can be expressed mathematically for constant density flow as

$$\int_{y_{surf}/c}^{y_{div}/c} \frac{u}{U_e} d\left(\frac{y - y_{surf}}{c}\right) = 0$$

where U_e is the boundary-layer edge velocity. The edge velocity was selected manually for each profile

using custom-written data-reduction software with a graphical user interface. Selection of the edge velocity also allowed for calculation of the boundary-layer displacement thickness,

$$\delta^*/c = \int_{y_{surf}/c}^{\delta/c} \left(1 - \frac{u}{U_e}\right) d\left(\frac{y - y_{surf}}{c}\right)$$

The momentum thickness was also calculated in the usual way, but with a simple modification for velocity profiles that may have reverse flow,

$$\theta/c = \int_{y_{surf}/c}^{\delta/c} \left| \frac{u}{U_e} \right| \left(1 - \frac{u}{U_e}\right) d\left(\frac{y - y_{surf}}{c}\right)$$

RESULTS AND DISCUSSION

The lift performance of the GLC-305 airfoil was affected differently by the two ice shapes considered in this investigation. As shown in Fig. 3, the maximum lift penalty for the airfoil with rime shape 212 was much less than for the glaze shape 944. The lift curves show that maximum lift was attained at about 11 deg. for the rime shape and at about 7 deg. for the glaze shape. (The lift performance and pressure data were taken from Addy *et al.*¹³ and were acquired without the traversing mechanism installed in the test section.) This information was used to select the angles of attack at which the flowfield data were acquired. The choice of 6, 8 and 10 deg. for the rime shape revealed the flowfield development leading up to stall. The analogous choices for the glaze shape were 0, 4 and 6 deg.

A comparison of the ice geometries in Fig. 1 shows that the glaze shape had a large “horn” that is oriented at a large angle relative to the airfoil chord line. In contrast, the rime shape had a geometry that could be considered as an extension of the airfoil leading edge. These differences in geometry determined the extent of separated flow aft of the ice shape. A comparison of clean and iced pressure distributions at matched angle of attack is shown in Fig. 4. The measured C_p distribution in the region of the rime and glaze ice shapes was not smooth owing to the roughness of the simulated ice. This is particularly evident on the lower surface for both ice shapes. The clean-airfoil pressure distribution was marked by a large suction peak of nearly -4.0 in C_p , followed by a very large adverse gradient. In the rime-ice pressure distribution, there was a suction peak of -2.5 in C_p at $x/c \approx -0.03$. This pressure tap was located near the tip of the ice shape, where a large, local flow acceleration was likely to occur. The short region of nearly constant pressure from $x/c \approx -0.02$ to $x/c \approx 0.01$ was indicative of a small

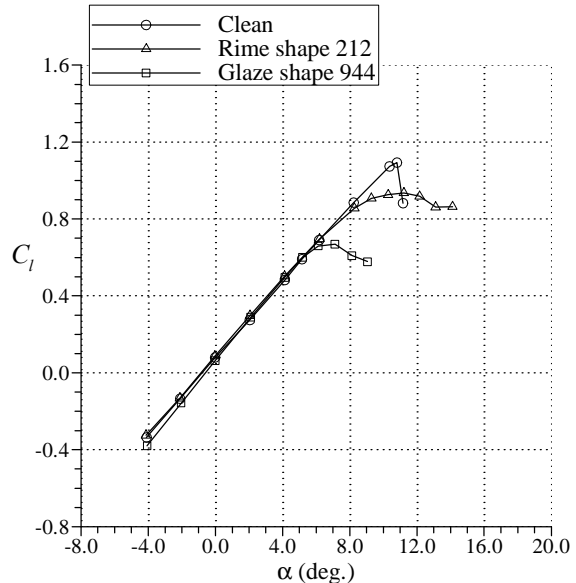


Fig. 3 Lift performance comparison of the GLC-305 airfoil with and without leading-edge ice-shape simulations at $M = 0.12$ and clean data at $Re = 3.0 \cdot 10^6$, iced data at $Re = 3.5 \cdot 10^6$, after Addy *et al.*¹³

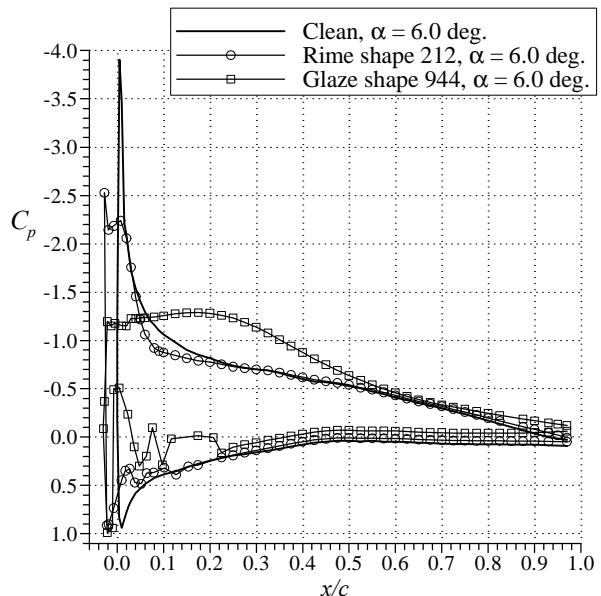


Fig. 4 Effect of ice simulations on surface pressure distribution at $M = 0.12$ and clean data at $Re = 3.0 \cdot 10^6$, iced data at $Re = 3.5 \cdot 10^6$, after Addy *et al.*¹³

separation bubble. The pressure recovery aft of this “plateau” indicates transition in the separated shear layer.⁴ That is, the start of transition occurred at the end of the plateau and start of the recovery regions. The shear-layer reattachment location can be approximated by the location where the iced-airfoil C_p intersects the clean airfoil C_p .^{4,5} In this case, the clean and iced pressure recovery regions overlap. The split-film flowfield data indicated that reattachment occurred at $x/c \approx 0.05$, which was slightly downstream of this overlap region. The pressure distribution for the airfoil with the glaze ice shape indicates that the separation bubble was much larger in this case. The region of nearly constant pressure on the upper surface extended to $x/c \approx 0.25$. The approximate shear-layer reattachment location, determined by the intersection of the clean and iced pressures was located at $x/c = 0.60$. This compares favorably to the location determined from the split-film flowfield measurements, $x/c = 0.53$. The divergence of the trailing-edge and lower-surface pressures also indicated that the airfoil was near stall.

An important concern in conducting the intrusive split-film measurements was the effect of the probe and support strut on the separated and reattaching flowfield. An analysis of the pressure distributions shows that this effect was likely small. Figure 5 shows a comparison of pressures for various chordwise probe locations. These are for the airfoil with the glaze ice shape at 4 deg. angle of attack. The data labeled “No Probe” were taken from the main chordwise row of pressure taps without the traversing mechanism, and the other three sets were taken from the chordwise row of taps located at the same spanwise station as the main vertical traverse strut. These pressures were acquired with the split-film probe located within 0.015-inch of the airfoil surface. As shown in the data, the presence of the probe and strut caused slightly larger suction pressures in the “plateau” region of the separation region. The beginning of the pressure recovery is not effected by the probe and strut. However, the recovery gradient became larger as the probe was moved farther upstream into the bubble region. This had the effect of slightly reducing the bubble size with the shear-layer reattachment being farther forward by a few percent chord. It should be noted that the faired probe holder was about 8% chord downstream of the probe tip. Since the probe was angled down toward the airfoil surface, the probe holder was always much farther above the surface. Its presence is observed in the pressure at $x/c = 0.40$ with the probe tip at $x/c = 0.30$. Its proximity to the surface caused a local flow acceleration resulting in the more negative C_p at this location. This effect was not observed as the probe tip was located farther upstream with the probe holder

located in the pressure recovery region. This minor effect of the probe and strut interference was comparable to that observed by Bragg *et al.*⁵ Khodadoust⁶ also compared split-film velocity data to non-intrusive LDV data and found very good agreement, further indicating that interference effects were small.

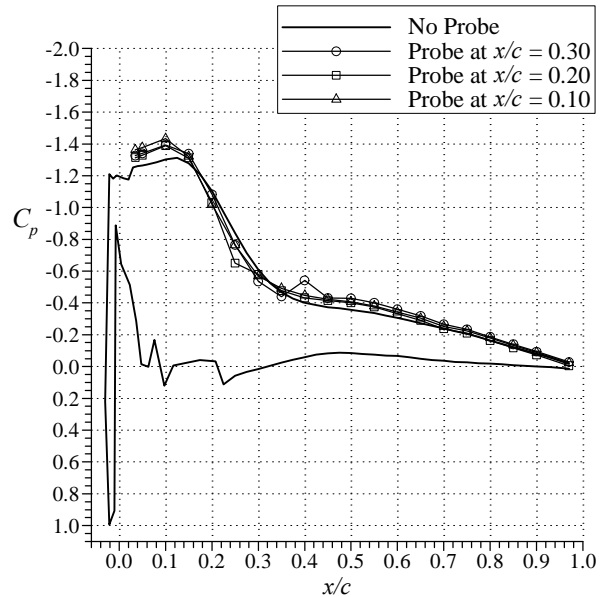


Fig. 5 Effect of probe and strut on surface pressure distribution for the glaze ice configuration 944 at a = 4 deg. with $Re = 3.5 \cdot 10^6$ and $M = 0.12$.

Flowfield Comparisons

Contour plots of the mean streamwise velocity provide a good overall illustration of the separated flow past the ice shape. An example of these data is shown in Fig. 6 for the airfoil with the glaze ice shape at 6 deg. angle of attack. The plot shows how the boundary-layer separated near the tip of the glaze ice horn. A significant reverse flow region formed below the separated shear layer. Reverse flow velocities as high as 40% of the freestream velocity were recorded inside the bubble. Outside of the bubble, streamwise flow velocities a factor of 1.6 larger than the freestream value were recorded. A strong shear layer divided these flow regions. The shear-layer thickness grew downstream of separation as transition occurred. No velocity data were acquired upstream of $x/c = 0.02$ directly aft of the ice horn, as indicated in Fig. 6. It is likely that the local flow in this region was very low-speed in either the upstream or downstream direction. The zero-velocity contour line shows that the mean

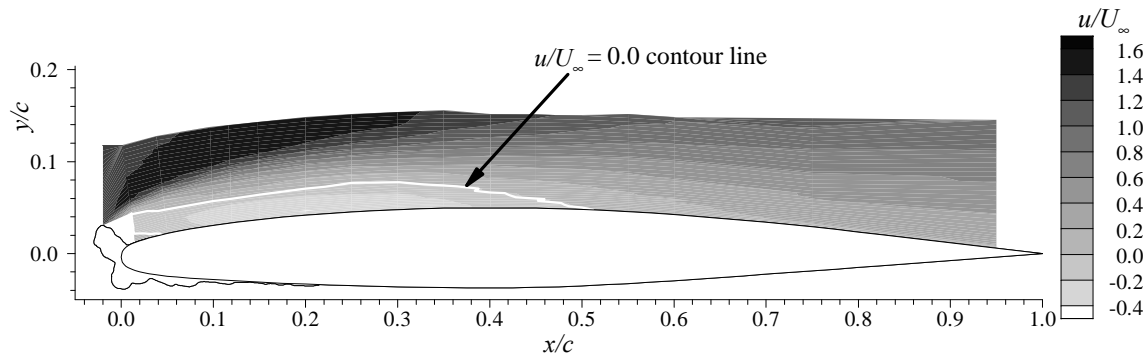


Fig. 6 Contour plot of mean streamwise velocity for the glaze ice configuration 944 at $\alpha = 6$ deg. with $Re = 3.5 \cdot 10^6$ and $M = 0.12$.

reattachment location was near $x/c = 0.53$. The developing turbulent boundary layer downstream of reattachment did not show evidence of separation up to $x/c = 0.95$, where the last profile was measured. While the contour plots provide an overall view of the complex flowfield, quantitative comparisons of the bubble characteristics are difficult to determine.

The stagnation and dividing streamline characteristics demonstrate more quantitative aspects of the separation bubble development. These are plotted in Fig. 7 for the rime ice shape and Fig. 8 for the glaze ice shape. Both sets of streamlines indicate the mean shear-layer reattachment location by the intersection of the streamline with the airfoil surface. For the airfoil with the rime shape, the increase in bubble size was nearly linear with increasing angle of attack, based upon the movement of reattachment locations. For the airfoil with the glaze shape, the bubble growth was much more non-linear with increasing angle of attack. The bubble approximately doubled in size from $\alpha = 0$ to 4 deg. and then nearly doubled in size from $\alpha = 4$ to 6 deg. The streamlines clearly illustrate the difference in aerodynamic severity between the two different ice shapes. The rime ice shape could be thought of as an extension of the airfoil leading edge. Since it was not smooth, a small bubble formed at 6 deg. angle of attack. The glaze shape, in contrast, had a large upper surface horn that was located downstream of the leading edge and had a large angle to the oncoming flow. This resulted in a much larger bubble at 6 deg. angle of attack and hence the impending stall. The bubble formed in the rime ice case at $\alpha = 10$ deg., was even smaller than for the glaze case at 6 deg. owing to this difference in geometry. These results reinforce previous performance results about the size and location of ice horn features.^{2,18}

The separation bubble reattachment locations determined from the streamline plots are summarized in Table 1. Also shown are the locations determined from the simple method of comparing the clean and iced pressure distributions. The data indicate that the pressure distribution method works well as an approximate method of determining reattachment even for these long bubbles. Thus, the data further support the conclusion of Bragg *et al.*⁵ in this regard.

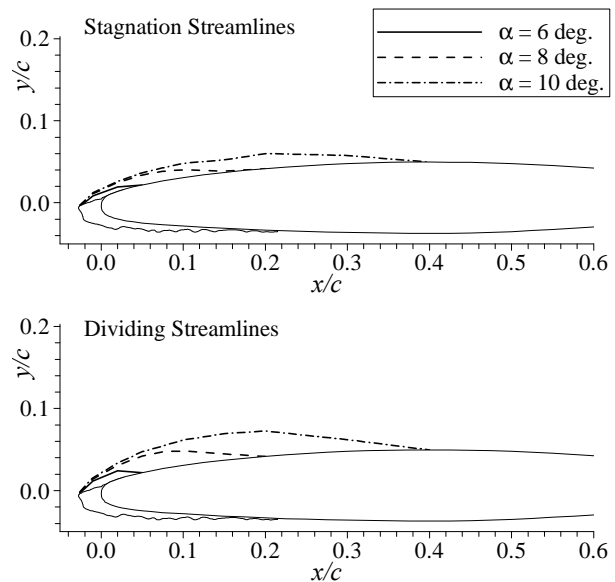


Fig. 7 Stagnation and dividing streamlines for the rime ice configuration 212 at $Re = 3.5 \cdot 10^6$ and $M = 0.12$.

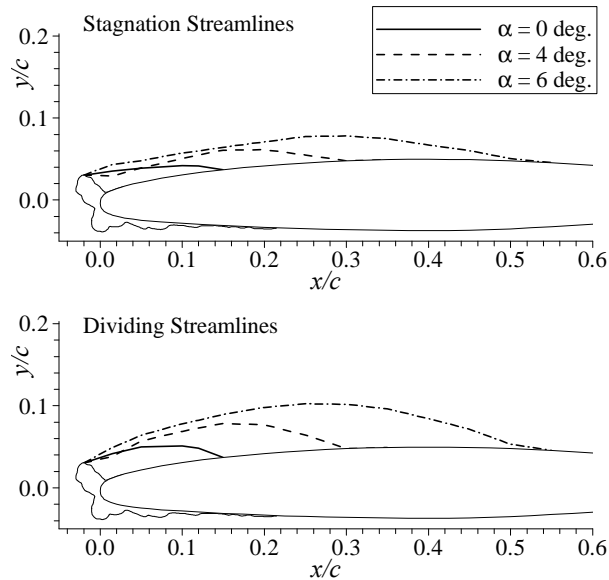


Fig. 8 Stagnation and dividing streamlines for the glaze ice configuration 944 at $Re = 3.5 \cdot 10^6$ and $M = 0.12$.

Table 1 Comparison of shear-layer reattachment locations at $Re = 3.5 \cdot 10^6$ and $M = 0.12$.

Ice Shape and Angle of Attack	Reattachment Locations, x/c	
	From Cp's	From Streamlines
Rime, $\alpha = 6$ deg.	0.04	0.05
Rime, $\alpha = 8$ deg.	0.20	0.18
Rime, $\alpha = 10$ deg.	0.45	0.40
Glaze, $\alpha = 0$ deg.	0.14	0.15
Glaze, $\alpha = 4$ deg.	0.31	0.30
Glaze, $\alpha = 6$ deg.	0.60	0.53

The integral boundary-layer parameters offer further comparison of these separation bubble characteristics. The displacement and momentum thicknesses are plotted for both shapes in Figs. 9 and 10. For the glaze ice shape case (Fig. 9), there was a large increase in displacement thickness from $x/c = -0.02$ to 0.02 . This trend was also observed by Bragg *et al.*,⁵ for a simulated glaze ice shape on a NACA 0012 airfoil and their data are plotted in Fig. 9 for comparison. The plot symbols were matched based on bubble size. The separation bubble length for $\alpha = 4$ deg. of Bragg *et al.*⁵ was similar to $\alpha = 0$ deg. in the present data. Likewise, the bubble length for $\alpha = 6$ deg. of Bragg *et al.*⁵ was similar to $\alpha = 4$ deg. in the present data. The agreement in these data for the $\alpha = 0/4$ deg. case is remarkably good, considering the differences in ice shape and airfoil geometry. These differences in

geometry likely caused the divergence in the two data sets downstream of $x/c = 0.15$, which coincides with the bubble reattachment location. It is likely that the pressure distributions were different downstream of this location, thus leading to differences in the turbulent boundary-layer development. For the $\alpha = 4/6$ deg. comparison, the agreement is also good up to $x/c = 0.15$. Downstream of this location the trend in the present data is consistent with the trend for the $\alpha = 0$ deg. case, whereas δ^*/c tends to level off for the Bragg *et al.*⁵ data. The reason for this is not clear, but may be related to changes in the flowfield close to stall. Maximum lift in both the present data and Bragg *et al.*⁵ occurred at 7 deg. Therefore, bubbles of similar sizes occurred at one degree below maximum lift for Bragg *et al.*,⁵ but three degrees below maximum lift for the present data. Unfortunately, no data downstream of $x/c = 0.35$ were available in the present case one degree below maximum lift (i.e., at $\alpha = 6$ deg.) to aid in this

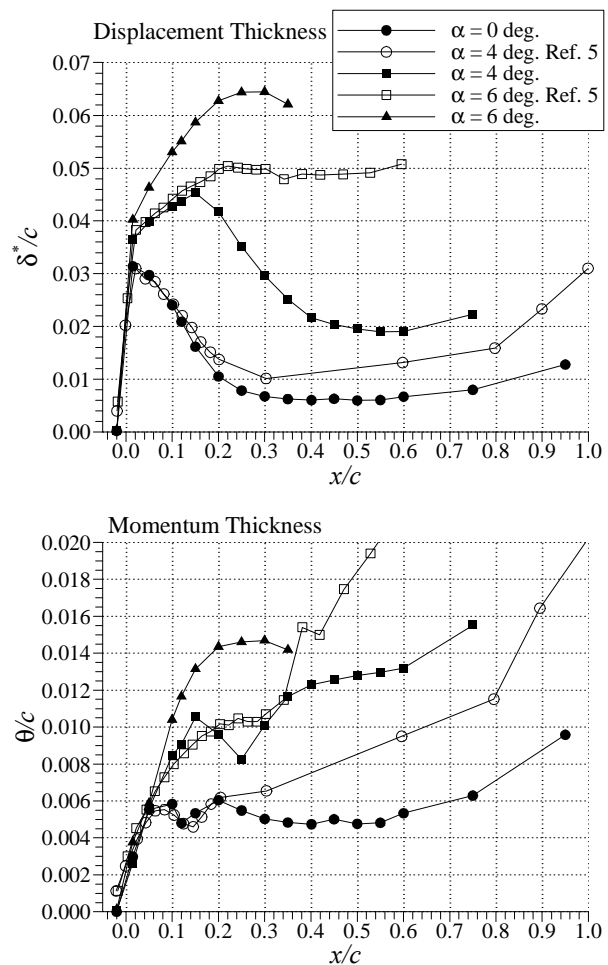


Fig. 9 Comparison of integral boundary-layer parameters for the glaze ice configuration 944 at $Re = 3.5 \cdot 10^6$ and $M = 0.12$.

interpretation. The data comparison in the $\alpha = 0/4$ deg. case do suggest that these large separation bubbles may have certain integral characteristics that are universally similar.

Analogous comparisons were also performed between the two data sets for the boundary-layer momentum thickness as shown in Fig. 9. As with the displacement thickness, the agreement is good for matched bubble sizes at $\alpha = 0/4$ deg. upstream of $x/c = 0.20$. Downstream of this location there was some divergence likely owing to the differences in geometry. Agreement is also good in the $\alpha = 4/6$ deg. case upstream of $x/c = 0.30$, except for the present data points at $x/c = 0.15$ and $x/c = 0.25$. The location $x/c = 0.30$ approximately corresponds to bubble reattachment for both data sets. Bragg *et al.*⁵ noted that for their $\alpha = 4$ deg. data, the first local maximum in momentum thickness corresponded to the shear-layer transition location as determined from the surface pressure distribution. In the present data (at $\alpha = 0$ deg.), the local maximum was located at $x/c = 0.10$. This is very close the transition location estimated from the surface pressure distribution. The local maxima at $x/c \approx 0.15$ and $x/c \approx 0.25$ for $\alpha = 4$ and 6 deg. in the present data also corresponded to the transition location determined from the surface pressure distribution. Bragg *et al.*⁵ also suggested that the shear-layer reattachment location could be determined by the second local maxima in the θ/c data, if present. This only occurred at $x/c = 0.20$ for $\alpha = 0$ deg. in the present data and this was downstream of reattachment which occurred at $x/c = 0.15$.

These integral boundary-layer parameters are plotted for the rime ice shape in Fig. 10. The smaller bubble sizes for this ice shape are clearly indicated by the much lower values of displacement thickness compared to the glaze ice case. Despite the differences in the magnitude of the values, the trends are very similar. There is a steep increase in δ^*/c from $x/c = -0.017$ to $x/c = 0.0$, this is followed by a reduced slope reaching a maximum value. Given the differences in the geometry of the ice shapes, the agreement in these trends further indicates universal similarities of the separation bubble characteristics. Analogous trends were also observed in the momentum thickness characteristics. For example, there are local maxima at $x/c = 0.02$ and $x/c = 0.08$, for $\alpha = 6$ and 8 deg., respectively. These locations approximately correspond to the start of the pressure recovery region of the surface pressure distribution, thus indicative of shear-layer transition. It is not clear from these data why a similar local maximum does not occur at $\alpha = 10$ deg.

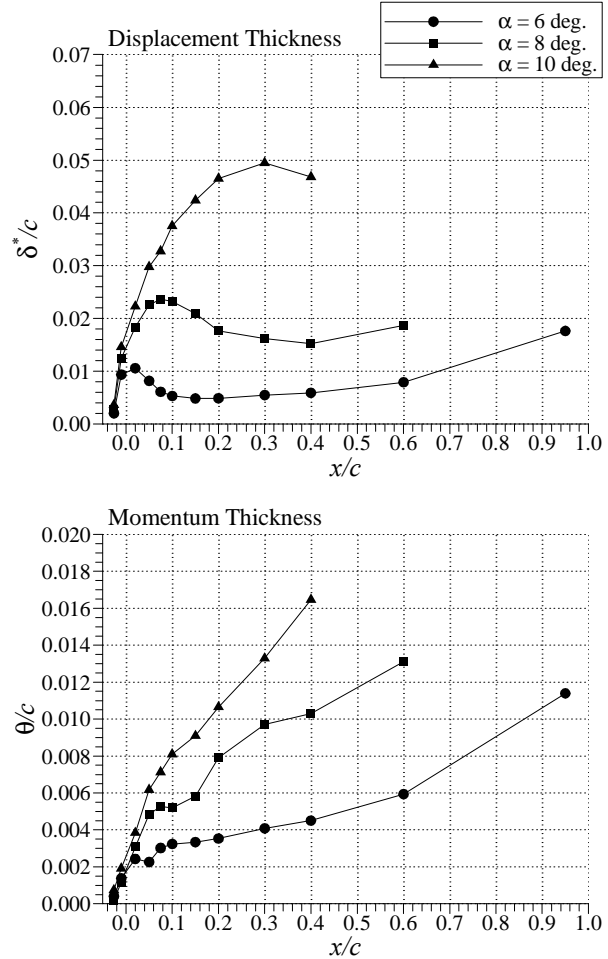


Fig. 10 Comparison of integral boundary-layer parameters for the rime ice configuration 212 at $Re = 3.5 \cdot 10^6$ and $M = 0.12$.

Reynolds and Mach Number Effects

The independent effects of Reynolds and Mach number on the separated flowfield development was also investigated. This was motivated by previous measurements that showed little change in the integrated performance coefficients and pressure distributions of the iced airfoil for large changes in Reynolds number.¹³ In fact, it was found that changes in Mach number had more of an effect on maximum lift than did changes in Reynolds number.¹³ An example of this effect is illustrated in Fig. 11. The plot shows how the maximum lift coefficient decreased slightly as the Mach number was increased. This drop in $C_{l,max}$ was about 8% between $M = 0.12$ and $M = 0.28$. A comparison with the lift data in Fig. 3 show virtually no difference in $C_{l,max}$ from $Re = 3.5 \times 10^6$ to 10.5×10^6 at $M = 0.12$. Similar trends were observed in the flowfields of the present study. For example, Fig. 12 shows a comparison of stagnation streamlines for three

Reynolds and Mach number combinations for the airfoil with glaze ice shape 944. For the $\alpha = 4$ deg. case, the bubble size is virtually identical across the three free-stream conditions. The apparent discrepancy between $x/c = 0.12$ and 0.24 for the $M = 0.21$ case occurred because no boundary-layer profiles were taken on this interval for this condition. For $\alpha = 6$ deg., the stagnation streamline for the $M = 0.21$ case indicates that the separation bubble was slightly larger than for the other conditions. This is consistent with the interpretation of the pressure distributions in Addy *et al.*¹³ and the present study that indicate larger bubble sizes at higher Mach numbers. It is reasonable that the larger bubble results in airfoil stall at a slightly lower angle of attack and lower lift coefficients. It is unclear what phenomenon causes the larger bubble sizes for higher Mach numbers.

The integral boundary-layer parameters also show very little influence of Reynolds and Mach numbers. These are plotted in Fig. 13 for the glaze ice case at $\alpha = 6$ deg. The larger bubble size observed in Fig. 12 for $M = 0.21$, is partially represented in the δ^*/c data at $x/c = 0.35$. Unfortunately, no displacement thicknesses could be calculated downstream of this location because the edge of the boundary layer was not measured. This was simply a limitation of the traversing mechanism. This effect is not observed in the momentum thickness data, however, it suffers from the same limitations downstream of $x/c = 0.35$. The discrepancy in θ/c values between $x/c = 0.12$ and 0.24 for the $M = 0.21$ case, is likely due to the lack of data for these locations.

A comparison of the velocity profiles is shown in Fig. 14. The profile at $x/c = 0.12$ shows the strong reverse flow velocities in the separation bubble region. There was good agreement in the velocity data across the three conditions up to the edge of the shear layer at $(y - y_{surf})/c = 0.07$, where the $M = 0.21$ velocities were slightly slower than the $M = 0.12$ data. The profiles downstream of this location show how the strength and size of the reverse flow region decreased up to $x/c = 0.55$ which was close to the mean reattachment location for this case. The vertical location above the surface where the $M = 0.21$ velocity data began to depart from the $M = 0.12$ data moved closer to the surface for profiles located farther downstream. Although it is difficult to see in Fig. 14, the profiles at $x/c = 0.55$ show that this location was downstream of mean reattachment for the $M = 0.12$ cases, but upstream of mean reattachment for $M = 0.21$. The velocity profiles at $x/c = 0.45$ and 0.55 also illustrate that the displacement thickness at $M = 0.21$ was likely larger than for the $M = 0.12$ cases, since the mean velocities were slower. Therefore, it is likely that the

displacement thicknesses downstream of $x/c = 0.35$ would continue to be larger at $M = 0.21$ than at $M = 0.12$.

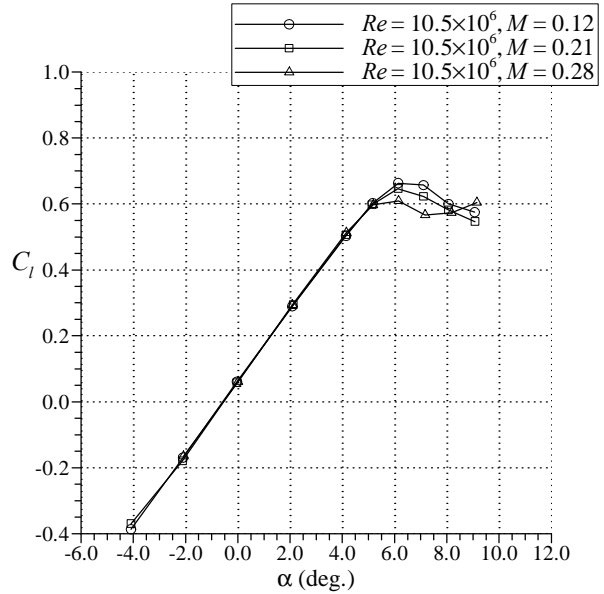


Fig. 11 Effect of Mach number on the lift performance of the GLC-305 airfoil with glaze ice configuration 944, after Addy *et al.*¹³

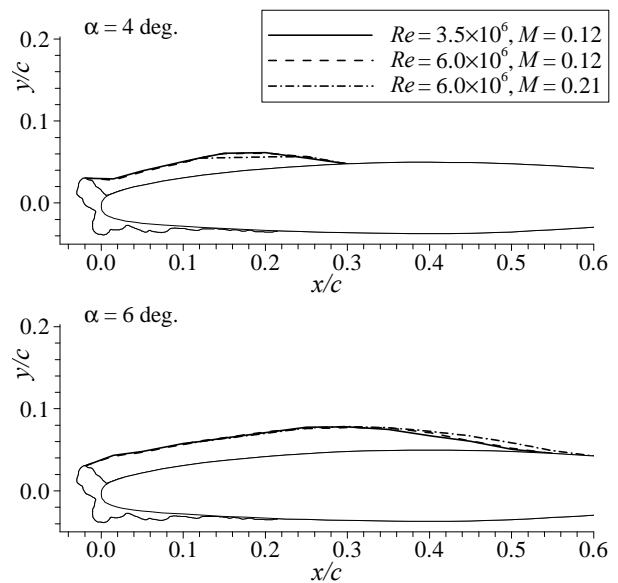


Fig. 12 Effect of Reynolds and Mach number on stagnation streamline locations for the glaze ice configuration 944.

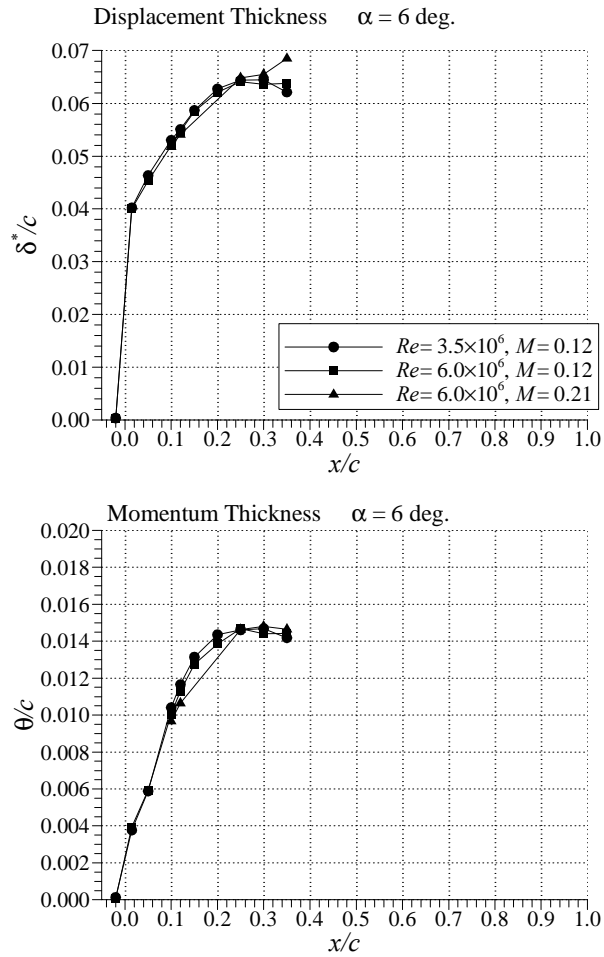


Fig. 13 Effect of Reynolds and Mach number on integral boundary-layer parameters for the glaze ice configuration 944 at $\alpha = 6$ deg.

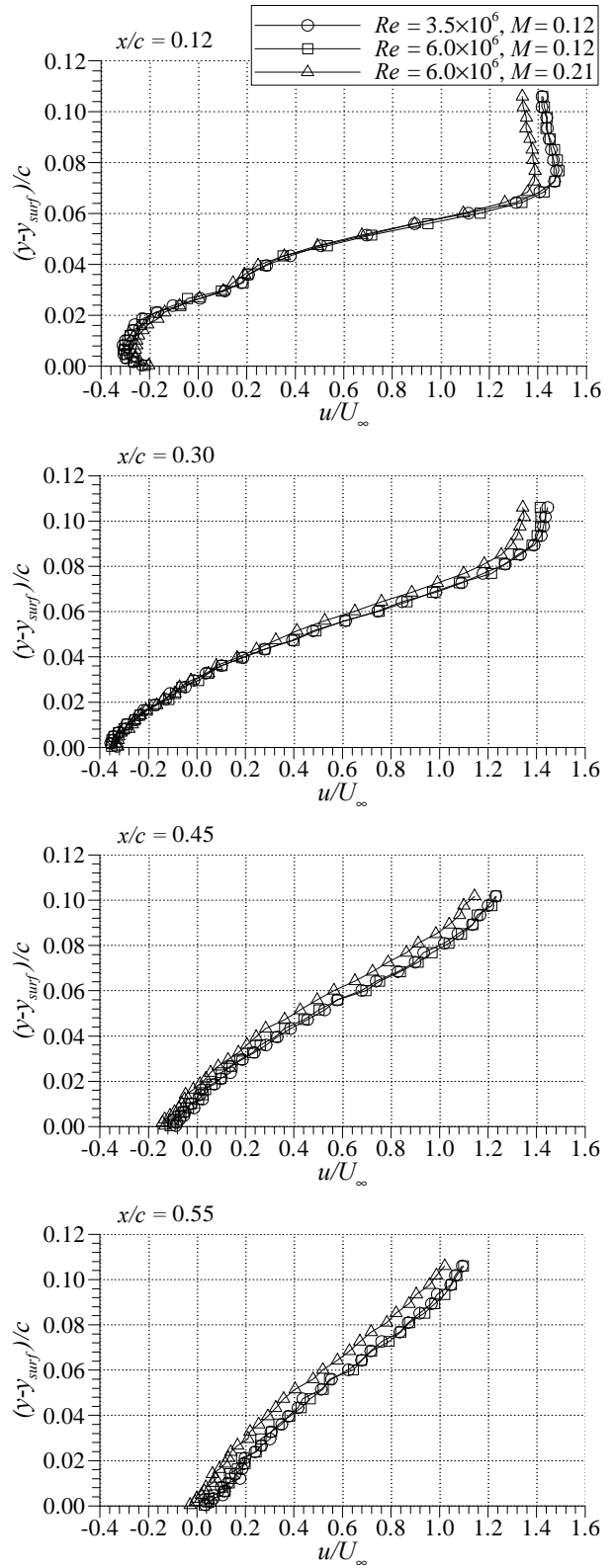


Fig. 14 Effect of Reynolds and Mach number on selected velocity profiles for the glaze ice configuration 944 at $\alpha = 6$ deg.

Turbulence Intensity Results

The turbulence intensity contours for the separated shear-layer regions were found to be in agreement with results from other separated flows. In this case the turbulence intensity was calculated as the root-mean-square of the fluctuating streamwise velocity and normalized by the freestream velocity. An example of these data is shown in Fig. 15 for the airfoil with the glaze ice shape at $\alpha = 6$ deg. This turbulence intensity contour corresponds to the velocity contour already discussed in Fig. 6. The maximum values, in the range of 0.32 to 0.36, occurred in the middle of the separated shear layer at $x/c \approx 0.30$. This region of peak turbulence intensity began just downstream of $x/c = 0.25$, which has already been identified as the shear-layer transition location from the pressure data. While difficult to see in the black and white contour plot, the u_{rms}/U_∞ levels in the range of 0.28 to 0.32 persist downstream to $x/c = 0.55$, the vicinity of reattachment. Downstream of reattachment the turbulence intensity levels decreased gradually, having peak values in the range of 0.20 to 0.24 at $x/c = 0.95$.

The trends and values of the turbulence intensity compare favorably with LDV measurements of the separation bubble flowfield past a NACA 0012 airfoil with simulated glaze ice accretion. Khodadoust⁶ reported peak values of $u_{rms}/U_\infty = 0.34$ in the vicinity of the separated shear-layer transition location. The general distribution of the turbulence intensity throughout the bubble flowfield was also very similar. Khodadoust noted that these values are in the range of those reported for separated flows downstream of a backward-facing step. For example, Eaton and Johnston¹⁹ state that local turbulence intensity values (u_{rms}/U_∞) near the center of the reattaching shear layer exceed 0.30. These large values have been attributed to large-scale and low-frequency perturbations of the

separated shear layer sometimes referred to as “flapping.”^{20,21} In the case of the backward-facing step, this vertical motion of the shear layer results in movement of the reattachment location. It is possible that similar unsteady characteristics may be present in the iced-airfoil case. Bragg *et al.*⁵ reported a low-frequency component in the spectra of the fluctuating shear-layer streamwise velocity. Likewise, Gurbacki and Bragg²² identified low-frequency components in the fluctuating pressure spectra in the separation bubble flowfield on an iced airfoil. The combined results of these studies suggest that a completely time-averaged representation of the flow may mask important details. This has implications for numerical modeling as well.

SUMMARY AND CONCLUSIONS

Flowfield measurements were performed on the upper surface of a GLC-305 airfoil configured with large glaze and rime ice-shape simulations. The mean and root-mean-square fluctuation of the streamwise velocity were acquired using a split-hot-film probe at several chordwise locations. These data were taken at three different angles of attack preceding stall for each iced-airfoil configuration. The freestream conditions were $Re = 3.5 \times 10^6$ and 6.0×10^6 at $M = 0.12$ and 0.21 . Integral boundary-layer parameters for these cases were calculated from the mean velocity profiles.

The velocity measurements confirmed the presence of large separation bubbles downstream of the ice shapes. For all cases measured, the separated shear layer reattached to the airfoil some distance downstream. No evidence of turbulent boundary-layer separation as far aft as $x/c = 0.95$ was found. The separation bubbles for the glaze ice configuration were much larger than those for the rime ice case, resulting from the differences in the horn geometry. Other than

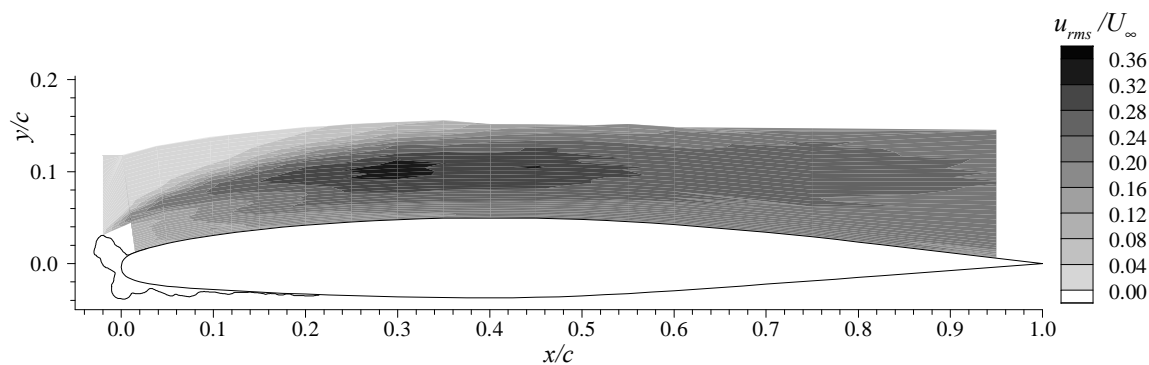


Fig. 15 Contour plot of turbulence intensity for the glaze ice configuration 944 at $\alpha = 6$ deg. with $Re = 3.5 \cdot 10^6$ and $M = 0.12$.

the differences in size, the integral boundary-layer characteristics were very similar. Analogous trends in the displacement thickness and momentum thickness were also observed and these were consistent with data from other experiments. Following the work performed by others, it was noted that local maxima in the momentum thickness distributions correlated well with the shear-layer transition location. These observations suggests that these large separation bubbles may have characteristics that are universally similar. Changes in Reynolds number did not significantly affect the separation bubble characteristics. However, a larger Mach number did result in a slightly larger separation bubble for the glaze ice case at $\alpha = 6$ deg. This result was consistent with previous observations of the airfoil surface pressure and performance data. The rms velocity distributions had peak values in the separated shear layer, downstream of transition, that compared well with previous work. These large values (on the order of 0.30 to 0.35 times the mean freestream velocity), indicate that potentially large-scale unsteadiness was present in the flowfield.

ACKNOWLEDGEMENTS

The authors wish to acknowledge several individuals who made significant contributions to this work. In particular, Joe Zoeckler and Carl Blaser from NASA Glenn played an important role in modifying and improving the traversing apparatus. Test engineers Pam Phillips and Bill Sewall and the experienced technicians of the NASA Langley LTPT deserve special recognition for their diligent efforts to make these sophisticated measurements successful. The LTPT staff played a collaborative role in upgrading the traverse apparatus and developing the split-film calibration facility. Finally, the authors at the University of Illinois were supported, in part, under NASA Grant NCC 3-852 from the John H. Glenn Research Center.

REFERENCES

- Lynch, F.T., and Khodadoust, A., "Effects of Ice Accretion on Aircraft Aerodynamics," *Progress in Aerospace Sciences*, Vol. 37, 2001, pp. 669-767.
- Lee, S., and Bragg, M.B., "Investigation of Factors Affecting Iced-Airfoil Aerodynamics," *Journal of Aircraft*, Vol. 40, No. 3, May-June, 2003, pp. 499-508.
- Bragg, M.B., Broeren, A.P., and Blumenthal, L.A., "Iced-Airfoil and Wing Aerodynamics," SAE Paper 2003-01-2098, Jun., 2003.
- Tani, I., "Low Speed Flows Involving Separation Bubbles," *Progress in Aeronautical Sciences*, Pergamon, New York, 1964, pp. 70-103.
- Bragg, M.B., Khodadoust, A., and Spring, S.A., "Measurements in a Leading-Edge Separation Bubble due to a Simulated Airfoil Ice Accretion," *AIAA Journal*, Vol. 30, No. 6, Jun. 1992, pp. 1462-1467.
- Khodadoust, A., "An Experimental Study of the Flowfield on a Semispan Rectangular Wing with a Simulated Glaze Ice Accretion," Ph.D. Dissertation, Dept. of Aeronautical and Astronautical Eng., Univ. of Illinois, Urbana, IL, 1992.
- Kerho, M.F., Bragg, M.B., and Shin, J., "Helium Bubble Flow Visualization of the Spanwise Separation on a NACA 0012 with Simulated Glaze Ice," AIAA Paper 92-0413, Jan. 1992.
- Bragg, M.B., Kerho, M.F., and Khodadoust, A., "LDV Flowfield Measurements on a Straight and Swept Wing with a Simulated Ice Accretion," AIAA Paper 93-0300, Jan. 1993.
- Gurbacki, H.M., and Bragg, M.B., "Unsteady Aerodynamic Measurements on an Iced Airfoil," AIAA Paper 2002-0241, Jan. 2002.
- Dunn, T.A., Loth, E., and Bragg, M.B., "Computational Investigation of Simulated Large-Droplet Ice Shapes on Airfoil Aerodynamics," *Journal of Aircraft*, Vol. 36, No. 5, Sept.-Oct. 1999, pp. 836-843.
- Pan, J., Loth, E., and Bragg, M.B., "RANS Simulations of Airfoils with Ice Shapes," AIAA Paper 2003-0729, Jan. 2003.
- Chung, J. J., and Addy, H.E. Jr., "A Numerical Evaluation of Icing Effects on a Natural Laminar Flow Airfoil," AIAA Paper 2000-0096, Jan. 2000.
- Addy, H.E. Jr., Broeren, A.P., Zoeckler, J.G., and Lee S., "A Wind Tunnel Study of Icing Effects on a Business Jet Airfoil," AIAA Paper 2003-0727, also NASA TM-2003-212124, Jan. 2003.

14. Von Doenhoff, A.E., and Abbott, F.T. Jr., "The Langley Two-Dimensional Low-Turbulence Pressure Tunnel," NACA TN 1283, May 1947.
15. McGhee, R.J., Beasley, W.D., and Foster, J.M., "Recent Modifications and Calibration of the Langley Low-Turbulence Pressure Tunnel," NASA TP 2328, July 1984.
16. Spaid, F.W., and Lynch, F.T., "High Reynolds Number, Multi-Element Airfoil Flowfield Measurements," AIAA Paper 96-0682, Jan. 1996.
17. Spring, S.A., "An Experimental Mapping of the Flowfield Behind a Glaze Ice Shape on a NACA 0012 Airfoil," M.S. Thesis, Dept. of Aeronautical and Astronautical Eng., Ohio State Univ., Columbus, OH, 1987.
18. Kim, H.S., and Bragg, M.B., "Effects of Leading-Edge Ice Accretion Geometry on Airfoil Aerodynamics," AIAA Paper 99-3150, 17th AIAA Applied Aerodynamics Conference, June 28-July 1, 1999.
19. Eaton, J.K. and Johnston, J.P., "A Review of Research on Subsonic Turbulent Flow Reattachment," *AIAA Journal*, Vol. 19, No. 9, Sept. 1981, pp. 1093-1100.
20. Simpson, R.L., "Aspects of Turbulent Boundary-Layer Separation," *Progress in Aerospace Sciences*, Vol. 32, 1996, pp. 457-521.
21. Driver, D.M., Seegmiller, H.L., and Marvin, J.G., "Time-Dependent Behavior of a Reattaching Shear-Layer," *AIAA Journal*, Vol. 25, No. 7, July, 1987, pp. 914-919.
22. Gurbacki, H.M. and Bragg, M.B., "Unsteady Flowfield About an Iced Airfoil," AIAA 2004-0562, Reno, NV, January 5-8, 2004.